


Cite this: *Mater. Adv.*, 2023,  
4, 4168

# Transport phenomena of TiCoSb: defect induced modification in the structure and density of states†

S. Mahakal,<sup>a</sup> Diptasikha Das,<sup>b</sup> Pintu Singha,<sup>c</sup> Aritra Banerjee,<sup>c</sup> S. C. Das,<sup>d</sup>  
Santanu K. Maiti,<sup>e</sup> S. Assa Aravindh<sup>f</sup> and K. Malik \*<sup>a</sup>

TiCoSb<sub>1+x</sub> ( $x = 0.0, 0.01, 0.02, 0.03, 0.04, \text{ and } 0.06$ ) samples have been synthesized, employing solid state reaction method followed by arc melting. Theoretical calculations, using density functional theory (DFT), have been performed to estimate the band structure and density of states (DOS). Further, energetic calculations using first principles have been carried out to reveal the formation energy for vacancy, interstitial and anti-site defects. A detailed structural calculation, employing Rietveld refinement, reveals the presence of embedded phases, vacancies, and interstitial atoms, which is also supported by theoretical calculations. Lattice strain, crystalline size, and dislocation density have been estimated by Williamson–Hall and modified Williamson–Hall methods. Thermal variation of resistivity [ $\rho(T)$ ] and thermopower [ $S(T)$ ] have been explained using the Mott equation and density of states (DOS) modification near the Fermi surface due to a Co vacancy and embedded phases. Figure of merit ( $ZT$ ) has been calculated and a  $ZT$  for TiCoSb 4 to 5 times higher than earlier reported values was obtained at room temperature.

Received 23rd June 2023,  
Accepted 7th August 2023

DOI: 10.1039/d3ma00323j

rsc.li/materials-advances

## 1. Introduction

Half-Heusler (HH) alloys are drawing the attention of researchers for their fascinating and unconventional physical properties along with their non-toxicity, good thermal stability, and high mechanical strength.<sup>1–6</sup> Research studies have been conducted to harness the interesting multinary properties with the unusual electronic and magnetic behaviour of HH alloys inside device applications.<sup>4,7–9</sup> HH compounds are extensively studied for their potential use in thermoelectric (TE) devices. HH alloys are attractive as mid-temperature TE materials for industrial waste heat recovery. Mid-temperature waste heat in industrial processes or automotive exhausts may be harnessed to convert heat into electricity using thermoelectric generators (TEGs) based on HH compounds.<sup>10–14</sup> HH alloy-based TE materials are used to

scavenge energy from ambient heat in portable power, *viz.*, wearable devices or remote sensors.<sup>15,16</sup> Zhu *et al.* have revealed that TE devices, made from HH alloys, are potential materials for TE cooling with high power density.<sup>17</sup> TE materials are used in aerospace for power generation or thermal management in space missions and unmanned aerial vehicles (UAVs) in the absence of traditional power sources.<sup>18–20</sup> HH alloy-based materials *viz.*, NiMnSb, CoMnSb, and FeMnSb based compounds also exhibit magnetic properties and suitable for applications in magnetic storage devices, spintronics, and magnetic sensors.<sup>21–23</sup> HH compound-based novel materials are not only used in TE power generation and spintronic devices but are also being explored as absorber layers in solar cells or as intermediate band materials to enhance the efficiency of photovoltaic devices.<sup>24</sup> Vacancies, present in the Heusler compound and valence electron count (VEC) are solely responsible for the novel electronic and magnetic properties of this group of materials. The crystal structure of the HH alloys depends on the constituent elements and changes with composition *viz.*, ZrNiSb, HfNiSb, and ScCoSb.<sup>25,26</sup> MCoSb [M = Ti, Zr, Hf] HH alloys are inter-metallic and crystallize as a MgAgAs cubic structure with space group  $F\bar{4}3m$ .<sup>27–31</sup> It may be considered as three inter penetrating face-centered cubic (fcc) lattice of almost identical unit cell volume. MCoSb is in the category of XYZ type HH alloy, where X is more electropositive than transition metal Y and main group Z element.<sup>30</sup> For MCoSb, one sublattice

<sup>a</sup> Department of Physics, Vidyasagar Metropolitan College, Kolkata-700006, India.  
E-mail: kartick.phy09@gmail.com

<sup>b</sup> Department of Physics, ADAMAS University, Kolkata-700126, India

<sup>c</sup> Department of Physics, University of Calcutta, Kolkata-700009, India

<sup>d</sup> Department of Physics, Tamkang University, New Taipei City-251301, Taiwan

<sup>e</sup> Physics and Applied Mathematics Unit, Indian Statistical Institute, 203

Barrackpore Trunk Road, Kolkata-700 108, India

<sup>f</sup> Nano and Molecular Systems Research Unit (NANOMO), University of Oulu, Oulu, FIN-90014, Finland

† Electronic supplementary information (ESI) available. See DOI: <https://doi.org/10.1039/d3ma00323j>



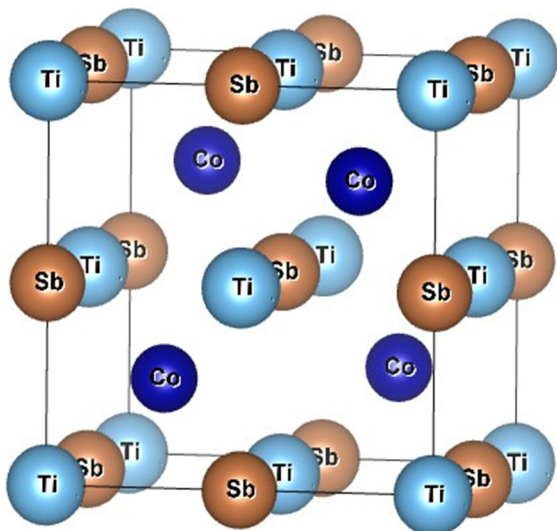


Fig. 1 Schematic view of the arrangements of Ti, Co, Sb atoms in TiCoSb half-Heusler alloy. Sky blue spheres represent Ti atoms, brown spheres represent Sb atoms, and navy blue spheres represent Co atoms.

consists of a lower valence transition metal, M, along with Sb sp atoms, and another one has been formed by a higher valence transition metal, Co, and vacancies. The materials exhibit semiconducting character in spite of the constituent element being metal.<sup>29,30</sup> The structure may be considered as an FCC lattice with X at the octahedral site ( $4a = (0, 0, 0)$ ). The structure is a combination of rock salt (XZ) and zinc blende (YZ) sub-lattice with Y at  $4c (\frac{1}{4}, \frac{1}{4}, \frac{1}{4})$  and Z at  $4b (\frac{1}{2}, \frac{1}{2}, \frac{1}{2})$ .<sup>30</sup> The  $4d (\frac{3}{4}, \frac{3}{4}, \frac{3}{4})$  site in  $F\bar{4}3m$  is filled for the  $XY_2Z$  Heusler alloy.<sup>30</sup> The tetrahedral site  $4d$  may be referred to as the interstitial site for the XYZ structure. A typical schematic diagram of a TiCoSb unit cell is presented in Fig. 1. The Wyckoff position of Ti, Co and Sb may also be considered at  $4c (\frac{1}{4}, \frac{1}{4}, \frac{1}{4})$ ,  $4a (0, 0, 0)$ ,  $4d (\frac{3}{4}, \frac{3}{4}, \frac{3}{4})$ , and vacant  $4b (\frac{1}{2}, \frac{1}{2}, \frac{1}{2})$  for the MgAgAs type structure.<sup>32</sup> The TiCoSb unit cell structure with vacant  $4d$  is more stable.<sup>32</sup> However, the constituent atoms and structure strongly corroborated with the electronic and transport properties of HH alloy. MCoSb is an 18 VEC-type material, and the Fermi level is just above the valence band.<sup>2,33–35</sup> Semiconducting properties in 18 VEC HH alloy arise due to the transfer of electron from the most electro positive X to the less electro positive Y and Z elements.<sup>30</sup> However, HH alloys having VEC = 18 may be understood from the Zintl chemistry framework. Close valence cell configuration is satisfied due to the transfer of valence electron from electro positive  $X^{n+}$  to covalent  $YZ^{n-}$  sub-lattice.<sup>30</sup> It is crucial to point out that electro negativity of X, Y, and Z site atoms lies in the range 1.2–1.7, 1.8–2.4, and 1.7–2.2, respectively.<sup>36</sup> A close cell configuration for the Y and Z atoms, *i.e.*,  $d^{10}$  and  $s^2p^6$  is achieved for the HH alloys.

Research in thermoelectric (TE) materials is emerging as a fascinating topic due to the potential alternative source of energy and peculiar physics involved in the technology.<sup>4,5</sup> Thermoelectricity converts thermal energy into electrical energy and *vice versa*. Until now, several systems have been studied as highly efficient TE materials *viz.*, PbTe based materials

( $ZT \sim 1.5$ ), chalcogenides [ $Bi_2Te_3$  ( $ZT \sim 1$ ),  $Sb_2Te_3$  ( $ZT \sim 1$ )],  $Mg_2Si$  ( $ZT \sim 1.4$ ), and oxide TE materials ( $ZT \sim 2.7$ ).<sup>30,37–39</sup> However, applications are limited by poor chemical, mechanical strength, and thermal stability.<sup>30</sup> TiCoSb is a potential TE material at mid-temperature.<sup>40</sup> MCoSb [M = Ti, Co, Sb] is a potential p-type TE material and efforts are on to enhance the efficiency by reducing thermal conductivity ( $\kappa$ ).<sup>27</sup> Large Seebeck coefficient ( $S(T)$ ) and electrical conductivity ( $\sigma$ ) due to d–d bonding near the Fermi surface make them attractive and a potential TE material. TiCoSb is paramagnetic and temperature independent.<sup>41</sup> Terada *et al.* have reported that it shows ferromagnetic behaviour due to different ferroelectric phase precipitations in the HH alloy matrix.<sup>41</sup> However, Iso-electronic alloying, defects, and disorder in the structure influence the electronic and transport properties, and concomitantly, the TE properties of the HH alloy.<sup>42</sup> TiCoSb shows a lower band gap of  $\sim 0.95$  eV amid the other iso-electronic alloys, ZrCoSb and HfCoSb.<sup>43</sup> Introduction of point defect at the X site and reduction of  $\kappa$  enhances the  $ZT \sim 1$  for n-type and p-type (MnInSn and MCoSb) HH Alloys.<sup>44</sup> Nano inclusion and complex iso-electronic alloying are also important routes to enhance the efficiency of a TE material.<sup>27,45</sup> Further,  $\kappa$  may be significantly reduced by point defects and disorder through phonon scattering. Iso-electronic alloying not only modifies electronic structure but also reduces  $\kappa$  by introducing point defects in the HH structure.<sup>45</sup> However, a nominal amount of impurities with 19 VEC HH alloy strongly affects the TE properties of the HH alloy.<sup>46</sup> But, scattering of a carrier with defects and disorder concomitantly reduces  $\sigma$ .<sup>47</sup> Xia *et al.* have described that short range order along with long range periodicity significantly enhance carrier conductivity accompanying the low  $\kappa$ .<sup>48</sup> Further, disorder also strongly affects the band structure of n-type MnInSn based HH alloy.<sup>49–51</sup> Effect of iso-electronic alloying and nano-inclusion in TE properties have been widely studied.<sup>27,40,45,52</sup> However, investigations on consequences of defect and disorder on crystal, electronic structure, and transport properties of TiCoSb are limited.<sup>53</sup>

Phase segregation in the HH alloy matrix is one of the important aspects of the TE study. In order to avoid the presence of second phases and defects, several methods have been implemented to synthesize TiCoSb HH alloy.<sup>54–56</sup> Sometimes, defects are favourable to enhance TE properties through modification in electrical and thermal transport properties.<sup>54,55</sup> However,  $ZT$  has been reduced due to segregation of the secondary phase *viz.*, CoSb in TiCoSb matrix.<sup>56</sup> M. Assad *et al.* have reported that embedded phases in doped TiCoSb enhance the  $ZT$  due to a reduction in  $\kappa_L$ .<sup>54</sup> C. S. Birkel *et al.* have synthesized TiCoSb in two different ways, mechanical alloying, and microwave synthesis. It has been observed that the second phase causes a reduction in TE properties.<sup>55</sup> Arc melting is one of the common techniques to synthesize HH or FH alloys. But the difference in melting points of constituent elements in the stoichiometry causes a source of defect/segregation in the HH alloy.<sup>54,56</sup> In order to avoid loss due to evaporation, there are instances of using extra Sb in TiCoSb stoichiometry.<sup>57</sup> However, the role of defects and second phases on the TE properties of



TiCoSb requires a systematic study. There is no meticulous investigation for the inclusion of extra Sb during the synthesis of TiCoSb and effect on TE properties due to the complex interplay of vacancies and embedded phases. Furthermore, this study may enlighten the source of defects, embedded phases in the synthesized matrix, and correlation with the transport properties of TiCoSb HH alloy.

Here we have reported the role of defects and precipitated phase on electronic structure and transport properties of polycrystalline TiCoSb alloy synthesized by solid state reaction followed by arc melting. In-depth structural characterizations have been performed using Rietveld refinement method from the X-ray diffraction (XRD) data. Occupancy and precipitated phase have been revealed from XRD. Vacancy in the synthesized materials has been shown schematically. Further, electronic band structure, DOS, and formation energy of TiCoSb have been estimated using density functional theory (DFT) calculation, considering the super cell structure. Effects of vacancy, interstitial defect, and anti-site defects have also been included in DFT calculations. Temperature dependent resistivity ( $\rho(T)$ ) and  $S(T)$  measurements have been carried out at low temperatures down to 10 K. Electron–electron (e–e) and electron–phonon (e–ph) coefficients have been estimated from the thermal variation of  $\rho(T)$  and  $S(T)$  data. The first time in-depth structural study using the refinement and correlation with low temperature transport properties has been presented in this article. Further, attempts have been made for theoretical calculation of band structure, density of states (DOS), and total energy per atom. Bipolar conduction has been found, according to the results obtained from transport properties and correlated with the structural parameters evaluated using Rietveld refinement. DOS has been tuned by modification in structural parameters and correlation with  $\rho(T)$ ,  $S(T)$  data have been elucidated, using the Mott equation. Theoretical and experimental data along with the estimated parameters have been corroborated in this endeavour.

In our present work, we have considered TiCoSb as a functional element for suitable energy conversion. TiCoSb<sub>1+x</sub> ( $x = 0.0, 0.01, 0.02, 0.03, 0.04, 0.06$ ) has been synthesized to study the role of defects and embedded phases in structural, transport, and electronic properties. The key findings of the present study are (i) Co vacancies in TiCoSb unit cell increase with Sb concentration, (ii) minute amount of CoTi and CoSb embedded phases have been revealed and supported by theoretical study, (iii) embedded phases, dislocation density, and strain are minimum, correspondingly maximum TiCoSb phase has been observed in TiCoSb<sub>1.02</sub>, (iv) modification in thermal variation of resistivity and thermopower is related with DOS due to Co vacancies, (v) inclusion of 2% extra Sb in TiCoSb stoichiometry during synthesis is sufficient to compensate the weight loss, and (vi) 4 to 5 times higher  $ZT$  than previously divulged for TiCoSb at room temperature has been obtained.

This paper is organized as follows. Section II describes precise steps for sample synthesis and characterizations to analyse the experimental results. Computational details for theoretical calculations have been presented in Section III. All the theoretical and

experimental results have been critically scrutinized and discussed in Section IV. Finally, conclusion and correlation have been drawn on the basis of theoretical and experimental results in Section V.

## II. Experimental details

Polycrystalline TiCoSb<sub>1+x</sub> ( $x = 0, 0.01, 0.02, 0.03, 0.04, 0.06$ ) samples were synthesized by solid state reaction. Weighted Ti (purity 99.998%; Alfa Aesar, UK), Co, and Sb (each of purity 99.99%; Alfa Aesar, UK) were arc melted at Argon atmosphere, and ingots were melted several times to obtain homogeneous alloy. The arc melted ingots were sealed in a quartz ampoule under pressure  $10^{-3}$  mbar for further treatment. Evacuated quartz ampoules were annealed at 1173 K for five days and then cooled down to room temperature at a cooling rate  $10^\circ\text{C hour}^{-1}$ . The prepared ingots were cut in rectangular shapes of dimension (1.5 mm  $\times$  2 mm  $\times$  5 mm) for measurement of transport properties. In order to carry out XRD measurements, prepared ingots were pulverised into fine powder. Structural characterization of the synthesized host phases, *i.e.*, TiCoSb, TiCoSb<sub>1.01</sub>, TiCoSb<sub>1.02</sub>, TiCoSb<sub>1.03</sub>, TiCoSb<sub>1.04</sub>, and TiCoSb<sub>1.06</sub> have been carried out by XRD using Diffractometer model: X'Pert Powder, PANalytical using Cu-K $\alpha$  radiation of wavelength 0.15406 nm. XRD has been carried out at room temperature in the range  $20^\circ \leq \theta \leq 80^\circ$  in  $\theta$ - $2\theta$  geometry. The Williamson–Hall and Modified Williamson–Hall methods have been employed to estimate lattice strain ( $\varepsilon$ ), crystal size ( $d$ ), and dislocation densities ( $N_D$ ) of the synthesized samples using the XRD data.<sup>58,59</sup> Further, in-depth structural analysis has been carried out by the Rietveld refinement technique using FullProf software.<sup>60</sup> Refinement analysis of the Bragg scattered TiCoSb<sub>1+x</sub> phases have provided exhaustive information on the long-range order in the host phase along with defects and disorder in the synthesized HH alloy structure. Further, mix-phase has been introduced during Rietveld refinements to investigate the presence of defects and embedded phases in the TiCoSb matrix.  $\rho(T)$  measurements of the synthesized polycrystalline alloys have been carried out using the conventional four probe method down to 10 K.  $S(T)$  measurements have been performed down to 20 K, employing standard differential technique.<sup>61–63</sup> TiCoSb is a HH alloy with a vacant 4d (3/4, 3/4, 3/4) and prone to antisite/interstitial defects. The defects have also been correlated with transport properties through modifications in the DOS of the synthesized samples. Embedded phases and defects in TiCoSb significantly alter the transport properties through carrier scattering and modification in electronic structure.

In order to corroborate the experimental findings, DFT calculations have been carried out using the plane wave pseudopotential code Vienna *Ab initio* Simulation Package (VASP).<sup>64</sup>

## III. Computational details

We have carried out DFT calculations for TiCoSb using the plane wave pseudopotential code VASP.<sup>64</sup> To expand the plane



waves included in the basis set, kinetic energy cut-off of 520 eV has been used. A generalized gradient approximation (GGA) has been employed in the Perdew Burke Erzenhof (PBE) formalism.<sup>65,66</sup> The atomic positions have been relaxed using energy and force tolerance of  $10^{-6}$  eV and  $0.001$  eV  $\text{\AA}^{-1}$ , respectively, to minimize the Hellmann–Feynmann forces. An fcc unit cell of TiCoSb has been optimized, and a relaxed lattice parameter of 5.88  $\text{\AA}$  has been found. A Monkhorst Pack K grid of  $4 \times 4 \times 4$  has been utilized for the Brillouin zone integration.

## IV. Results and discussion

The band structure and DOS have been presented in Figs. 2(a) and (b), respectively. A direct band gap of about 1.03 eV at the gamma point has been obtained. The DOS calculation has shown that the valence band maximum and conduction band minimum have mainly constituted from the contribution of Co and Ti orbitals, respectively.

We have simulated a super-cell of TiCoSb, containing 48 atoms using the optimized lattice parameter of the unit cell. In this super-cell, vacancies, interstitials, and anti-sites have been introduced. The total energy per atom of these super-cells is presented in Table 1. The energetic calculations have shown that the super-cell containing Co vacancy is more stable than that of Ti and Sb. Further, the system with Ti in the interstitial position is more stable than Co and Sb. We have also carried out calculations by introducing Co and Sb in the Ti position and found that the latter is more stable. The total energy per atom, calculated for the TiCoSb super-cell with 48 atoms, has also been shown for comparison. It is shown that having an interstitial Ti atom is closer in stability to the perfect structure.

Fig. 3 represents the XRD pattern of TiCoSb<sub>1+x</sub> ( $x = 0.0, 0.01, 0.02, 0.03, 0.04, 0.06$ ) samples synthesized by solid state reaction method. XRD has shown that the bulk matrices of the synthesized samples have crystallised in a cubic MgAgAs type structure. All the diffraction peaks have been indexed to

the corresponding structure and space group ( $F\bar{4}3m$ , No. 216) (Fig. 3). The effect of Sb concentrations on the most intense peak (220) has been demonstrated in Fig. 3 (inset) (220). XRD peaks shift towards a higher  $2\theta$  angle for  $0 \leq x \leq 0.04$ , indicating a reduction in unit cell volume. However, a large shift of the (220) peak towards a lower angle has been observed for  $x = 0.06$ . Any extra impurity peak has not been found in the XRD detection level. The full width at half maxima (FWHM) of (220) peaks has been estimated and presented in Fig. 4. FWHM of the synthesized samples decreases for  $0 \leq x \leq 0.02$ , indicating enhancement of crystal quality as HH alloy. An increase in Sb, *i.e.*, for  $0.02 \leq x \leq 0.06$ , increase in FWHM represents degradation of crystal quality. However, structural disorder, defects, and degradation of crystal quality may arise owing to the inherent off-stoichiometry and embedded phase.

In order to estimate in-depth structural parameters, Rietveld refinement analysis has been carried out using Fullprof software.<sup>60</sup> Further, the presence of embedded phases has been revealed by introducing a mix-phase Rietveld analysis. The CoTi and CoSb phases have been incorporated during Rietveld refinement, which improves the fitting quality, and reduces  $\chi^2$  (goodness of fit). However, reports on in-depth structural analysis of TiCoSb using Rietveld analysis are limited. But till date, no effort has been made to reveal the effect of Sb on structural and transport properties of the TiCoSb alloy using mix-phase Rietveld refinement. The experimental XRD patterns along with the theoretical fitted curve after Rietveld analysis are given in Fig. S1 (ESI†). Lattice parameter ' $a$ ' of the synthesized samples has been estimated, and  $a \sim 0.5883$  nm has been obtained for TiCoSb<sub>1+x</sub> ( $0 \leq x \leq 0.06$ ) samples. Value of ' $a$ ' parameter is in good agreement with the theoretically obtained value. A similar value of ' $a$ ' parameter has also been reported by Webster and Ziebeck ( $a = 0.5884$  nm).<sup>67</sup> Unit cell volumes of the synthesized samples have been estimated and presented in Fig. 5(a). Unit cell volume gradually decreases with increasing Sb concentration for  $0 \leq x \leq 0.04$  and increases for  $x = 0.06$ ,

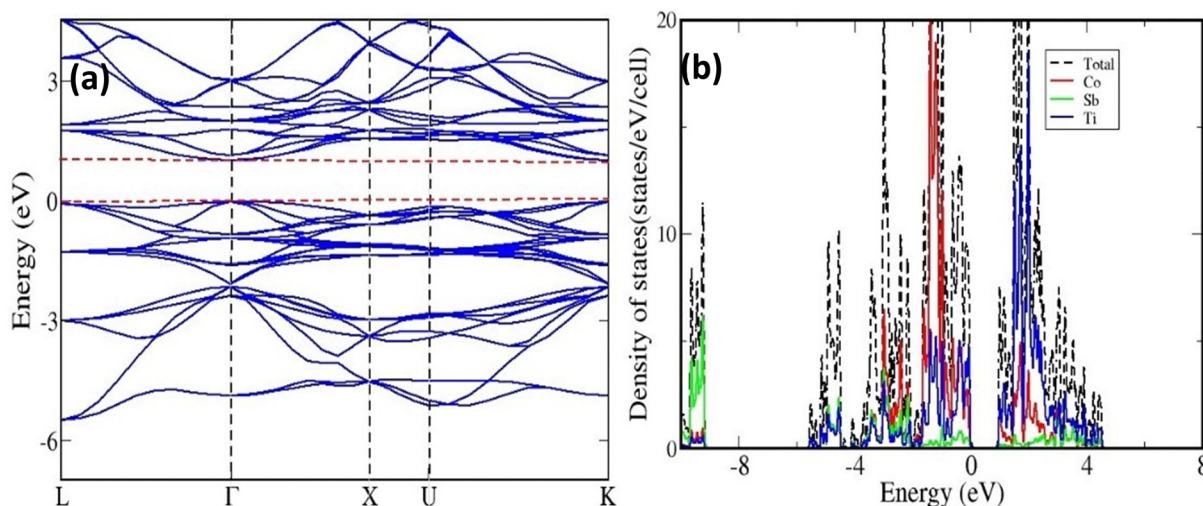


Fig. 2 Electronic (a) band structure and (b) DOS of TiCoSb half-Heusler alloy.



Table 1 The simulated total energy/atom for supercell containing vacancies, anti-sites, and interstitials

	TiCoSb	Vacancy			Interstitial			Antisite	
Energy (eV)	-6.96	$V_{\text{Ti}}$ -6.72	$V_{\text{Co}}$ -6.77	$V_{\text{Sb}}$ -6.76	Ti -6.94	Co -6.93	Sb -6.78	Ti-Co -6.82	Ti-Sb -6.86

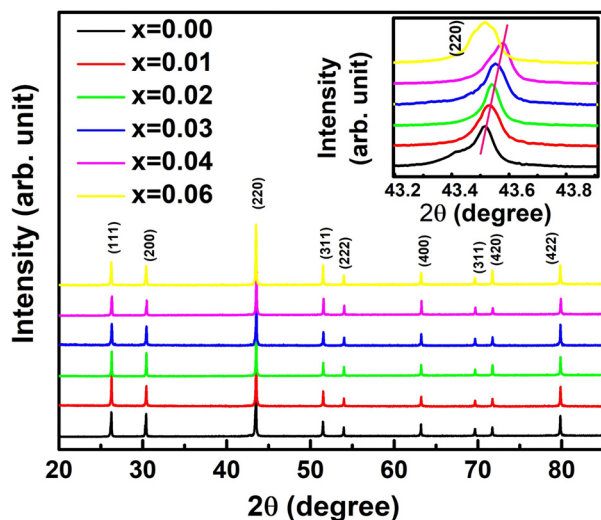


Fig. 3 X-ray diffraction pattern of synthesized  $\text{TiCoSb}_{1+x}$  ( $x = 0.0, 0.01, 0.02, 0.03, 0.04, 0.06$ ) polycrystalline materials (Inset shows position of highest intense (220) peak).

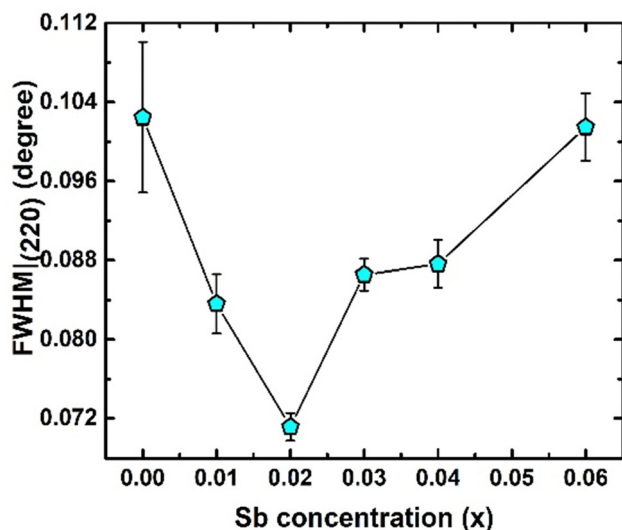


Fig. 4 Variation of Full Width at Half Maxima (FWHM) with Sb concentration for  $\text{TiCoSb}_{1+x}$  ( $x = 0.0, 0.01, 0.02, 0.03, 0.04, 0.06$ ). FWHM have been obtained by fitting the highest intense x-ray diffraction peak (220).

corroborated with (220) peak shift in the XRD pattern (Inset Fig. 3).

In-depth mix phase Rietveld analysis has revealed the presence of a minute amount of CoTi and CoSb phases in the synthesized  $\text{TiCoSb}_{1+x}$  matrix. Sb concentration-dependent weight percentage (wt%) of all the existing phases in the

synthesized  $\text{TiCoSb}$  samples are depicted in Fig. 5(b). wt% of CoTi phase decreases and CoSb phase increases gradually with Sb concentration in  $\text{TiCoSb}$  samples. A maximum  $\text{TiCoSb}$  phase as high as  $\sim 99\%$  has been achieved for  $x = 0.02$ . Phase segregations have been frequently observed in ternary, intermetallic  $\text{TiCoSb}$ -based HH alloys due to large differences in specific gravity and boiling points (Sb:  $1587^\circ\text{C}$ , Ti:  $1668^\circ\text{C}$ , Co:  $1495^\circ\text{C}$ ) of the constituent elements.<sup>44</sup> Evaporation of Sb during the arc melting of weighted elements in  $\text{TiCoSb}$  samples is one of the key reasons for the segregation of phases in the HH alloy host matrix.<sup>68</sup> Deviation from the chemical composition of  $\text{TiCoSb}$  during synthesis may lead to the presence of CoTi-embedded phases and structural disorder in the prepared samples.<sup>68</sup> A meticulous investigation has revealed that the variation of wt% of  $\text{TiCoSb}$ , CoTi, and CoSb phases with Sb concentration is associated with a slope change at  $x = 0.02$ . wt% of the host phase  $\text{TiCoSb}$  rapidly decreases after  $x = 0.02$ . Further, systematic Co vacancy in the synthesized  $\text{TiCoSb}$  samples has been revealed using the Rietveld refinement and a schematic representation is provided in Fig. 6 by employing Vesta software.<sup>69</sup> Co vacancy gradually increases with Sb concentration in  $\text{TiCoSb}_{1+x}$  ( $0 \leq x \leq 0.06$ ). The decrease in lattice volume of the synthesized sample may be related to ( $0 \leq x \leq 0.04$ ) increasing Co vacancy in the system. Das *et al.* have reported that Te vacancy-mediated point defects in  $\text{Sb}_2\text{Te}_3$  TE material cause a decrease in unit cell volume.<sup>70</sup> However, a jump in lattice volume for the  $\text{TiCoSb}_{1.06}$  sample has been observed. Primarily, Co vacancies have been created in the  $\text{TiCoSb}$  system as observed from Rietveld refinement analysis, and CoSb phases have formed in reaction with extra Sb. Further, the increase of Sb in  $\text{TiCoSb}$  may cause the presence of interstitial atoms and anti-site defects simultaneously. There are two possibilities arising due to the increase of Sb in  $\text{TiCoSb}$ ; Sb atom either goes into the interstitial site, *i.e.*,  $4d(\frac{3}{4}, \frac{3}{4}, \frac{3}{4})$  or simultaneously, Ti atom goes into the interstitial vacant  $4d(\frac{3}{4}, \frac{3}{4}, \frac{3}{4})$  position and Sb atom occupies Ti site, *i.e.*,  $\text{Sb-Ti}(\text{Sb}_{\text{Ti}})$  anti-site defect. According to the theoretical calculations, Ti at the interstitial position is more favourable than other configurations, and  $\text{Sb}_{\text{Ti}}$  anti-site is more stable than other anti-site defects. Interstitial Ti atoms in the  $\text{TiCoSb}$  unit cell causes an increase in lattice volume for  $x = 0.06$  and decrease in CoTi embedded phases in the  $\text{TiCoSb}$  matrix (Fig. 5). This result has been also corroborated with the peak shift in the XRD pattern in Fig. 3. XRD peak (220) shifts towards a higher angle for  $0 \leq x \leq 0.04$  compared to the  $\text{TiCoSb}$  sample [Fig. 3(inset)] owing to the collective diffraction from the embedded (segregated) phases and decreasing disorder, suggesting that the lattice constant has contracted. Whereas (220) peak shifts towards a lower angle for  $x = 0.06$  and is related to an increase in unit cell



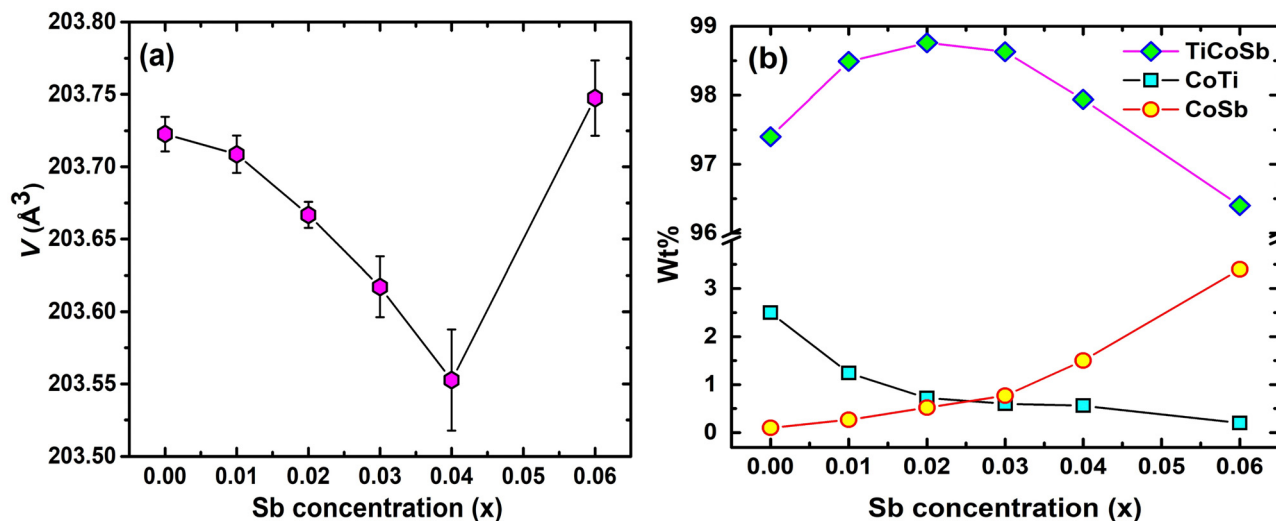


Fig. 5 Sb concentration dependent (a) unit cell volume and (b) Wt% of TiCoSb and embedded CoTi, CoSb phases, as obtained by employing Rietveld refinement of XRD data of synthesized  $\text{TiCoSb}_{1+x}$  ( $x = 0.0, 0.01, 0.02, 0.03, 0.04, 0.06$ ) polycrystalline sample.

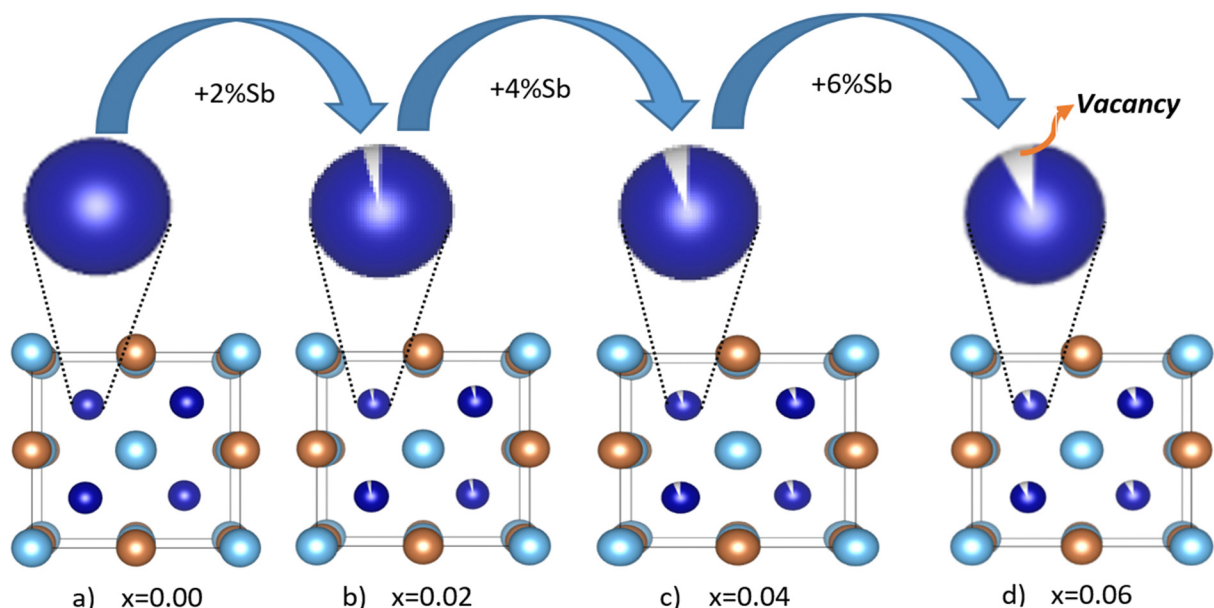


Fig. 6 Schematic representation of the formation of vacancy in  $\text{TiCoSb}_{1+x}$  ( $x = 0.0, 0.01, 0.02, 0.03, 0.04, 0.06$ ) polycrystalline samples, obtained from Rietveld refinement, using Vesta software. Sky blue spheres represent Ti atoms, brown spheres represent Sb atoms, and navy blue spheres represent Co atoms. The white region in Co atoms (zooming view) represents vacancy.

volume due to interstitial Ti atoms. Further, Rietveld refinement has been employed to estimate the Debye–Waller factor ( $B_{\text{iso}}$ ) related to positional disorder. The effect of extra Sb on  $B_{\text{iso}}$  of the synthesized samples ( $\text{TiCoSb}_{1+x}$ ) is presented in Fig. 7. A non-monotonic variation of  $B_{\text{iso}}$  with Sb concentration has been observed and anomaly for  $x = 0.02$  has been corroborated with other structural data *viz.*, FWHM of the XRD peak, unit cell volume, and estimated wt% of embedded phases. The Debye equation may be applied to estimate Debye temperature ( $\theta_{\text{D}}$ ) if the harmonic approximation, *i.e.*, the cubic and monoatomic

structure is considered.  $\theta_{\text{D}}$  and  $B_{\text{iso}}$  are related with the following equation within harmonic approximation<sup>71</sup>

$$B_{\text{iso}} = \left[ \frac{6h^2}{MK_{\text{B}}\theta_{\text{D}}} \right] \left[ \frac{1}{4} + \left( \frac{T}{\theta_{\text{D}}} \right)^2 \int_0^{\frac{\theta_{\text{D}}}{T}} \frac{x}{e^x - 1} dx \right] \quad (1)$$

where,  $M$  and  $T$  are mass and temperature, respectively. Non-monotonic variation of  $\theta_{\text{D}}$  of the prepared samples has been presented in Table 2 and lowest  $\theta_{\text{D}}$  ( $\theta_{\text{D}} = 357$  K) has been observed for the  $\text{TiCoSb}_{1.02}$  sample. Skovsen *et al.* have also



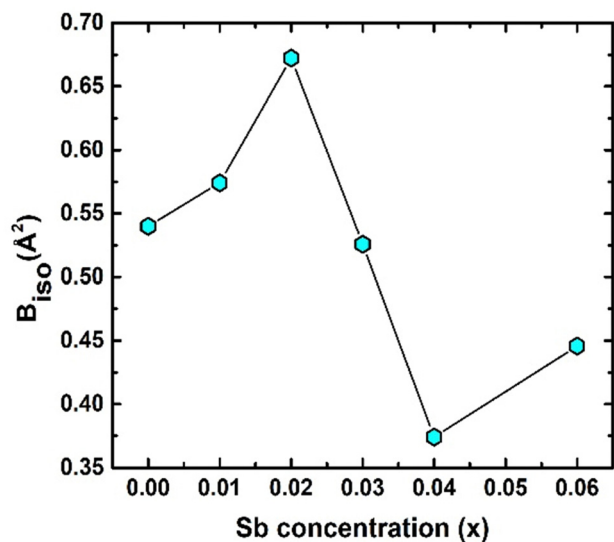


Fig. 7 Variation of Debye–Waller factor ( $B_{iso}$ ) with Sb concentration of synthesized  $\text{TiCoSb}_{1+x}$  ( $x = 0.0, 0.01, 0.02, 0.03, 0.04, 0.06$ ) polycrystalline materials.  $B_{iso}$  have been obtained from the Rietveld refinement of XRD data.

reported a similar value of  $\theta_D \sim 357$ .<sup>72</sup> Further,  $\theta_D \sim 417$  K has been estimated and reported by T. Sekimoto *et al.* employing measurement of longitudinal and shear velocities using the ultrasonic piles-echo method.<sup>73</sup>

Non-monotonic variation of  $\varepsilon$  and  $d$  of the synthesized samples is depicted in Fig. 8. The Williamson–Hall method has been employed to estimate  $\varepsilon$  and  $d$  using the relation<sup>58</sup>

$$\beta \cos \theta = \frac{K\lambda}{d} + 4\varepsilon \sin \theta. \quad (2)$$

Estimated  $\varepsilon$  for all  $\text{TiCoSb}_{1+x}$  ( $x = 0, 0.01, 0.02, 0.03, 0.04, 0.06$ ) samples is negative in nature, indicating compressive strain<sup>74</sup> (Please find supplementary Fig. S2 for Williamson–Hall plot, ESI†). The variations of  $\varepsilon$  and  $d$  with the Sb concentration of the synthesized samples are dissimilar in nature. The magnitude of  $\varepsilon$  is minimum and  $d$  is maximum for  $x = 0.02$  amid  $\text{TiCoSb}_{1+x}$  ( $x = 0, 0.01, 0.02, 0.03, 0.04, 0.06$ ) synthesized samples. It may arise due to the lowest wt% of embedded phases *viz.*, CoTi, CoSb, and maximum TiCoSb phase in  $\text{TiCoSb}_{1.02}$ . However, the highest  $d$  for the  $\text{TiCoSb}_{1.02}$  sample may be explained in light of the well-known Hall–Petch formula. According to the Hall–Petch formula, the strengthening effect of grain boundaries may be described as<sup>75–77</sup>

$$\sigma_{GB} = k_y d^{-1/2} \quad (3)$$

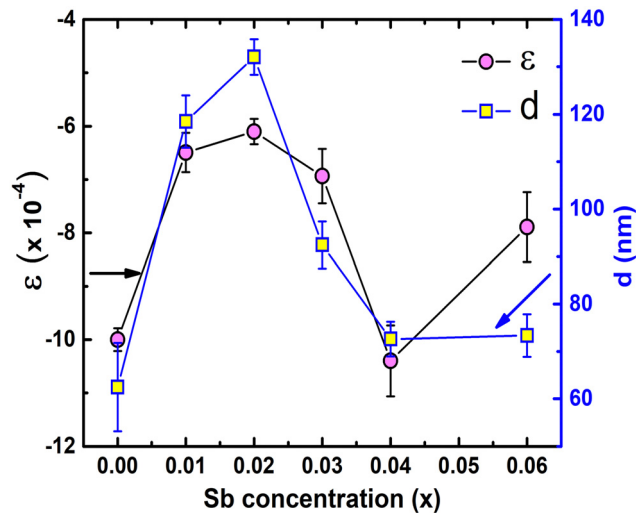


Fig. 8 Sb concentration dependent lattice strain ( $\varepsilon$ ) and crystalline size ( $d$ ) of  $\text{TiCoSb}_{1+x}$  ( $x = 0.0, 0.01, 0.02, 0.03, 0.04, 0.06$ ) polycrystalline materials, obtained from x-ray diffraction data using Williamson–Hall equation.

where  $\sigma_{GB}$ ,  $d$ ,  $k_y$  are yield strength at grain boundaries, crystalline size, and a material-dependent constant, respectively. Lattice mismatch at the grain boundary due to embedded phases may cause low  $\sigma_{GB}$  and high  $d$  value for  $\text{TiCoSb}_{1.02}$ . Modified Williamson–Hall plot has been used to carry out the calculation for estimation of  $N_D$  in  $\text{TiCoSb}_{1+x}$  ( $x = 0, 0.01, 0.02, 0.03, 0.04, 0.06$ ) samples, employing the relation<sup>59,78</sup>

$$\Delta K = 0.9/\delta + \frac{\pi A^2 B_D^2}{2} N_D^{1/2} K^2 C \pm O(K^4 C^2). \quad (4)$$

$K [= 2 \sin \theta_B / \lambda]$  and  $\Delta K [= \Delta(2\theta_B) \cos \theta_B / \lambda]$  parameters have been estimated from XRD data, where  $\theta_B$  is the Bragg angle,  $\Delta(2\theta_B)$  is the FWHM of the corresponding diffraction peak at  $\theta_B$  and  $\lambda$  ( $= 0.15406$  nm) is the wavelength of Cu-K $\alpha$  X-ray.  $N_D$  has been obtained from the slope of ' $\Delta K$  versus  $K^2 C$ ' curve, where  $C$  is average dislocation contrast factor. The ' $\Delta K$  versus  $K^2 C$ ' plots of the synthesized  $\text{TiCoSb}_{1+x}$  ( $x = 0.0, 0.01, 0.02, 0.03, 0.04, 0.06$ ) samples have been given in the ESI† (Fig. S3). Further, XRD data may be employed to estimate the dislocation density ( $N_D$ ) in the synthesized materials. The  $N_D$  of the synthesized samples ( $\text{TiCoSb}_{1+x}$ ;  $x = 0.0, 0.01, 0.02, 0.03, 0.04, 0.06$ ) has been estimated with respect to the  $\text{TiCoSb}$  (*i.e.*,  $x = 0.00$ ) sample. Non-monotonic behaviour of relative dislocation density ( $N_D/N_D|_{x=0}$ ) as a function of Sb concentration ( $x$ ) has been depicted in Fig. 9.  $N_D$  increases on either side of the point  $x =$

Table 2  $B_{iso}$ ,  $\theta_D$ ,  $\kappa_e$ ,  $\kappa_{tot}$ ,  $\rho$ ,  $S$ ,  $ZT$  of  $\text{TiCoSb}_{1+x}$  ( $x = 0.0, 0.01, 0.02, 0.03, 0.04, 0.06$ ) polycrystalline materials with different extra wt% Sb concentration ( $x$ ) at room temperature

Sb concentration (x).	$B_{iso}$ ( $\text{\AA}^2$ )	$\theta_D$ (K)	$\kappa_e$ ( $\text{W m}^{-1} \text{K}^{-1}$ )	$\kappa_{tot}$ ( $\text{W m}^{-1} \text{K}^{-1}$ )	$\rho_{300\text{K}}$ ( $\mu\Omega \text{m}$ )	$S_{300\text{K}}$ ( $\mu\text{V K}^{-1}$ )	$ZT_{300\text{K}}$
0.00	0.53	287	0.01339	4.945	536.54	−4.5	$9.6 \times 10^{-6}$
0.01	0.57	378	0.02308	4.6185	283.42	−44.5	$8 \times 10^{-4}$
0.02	0.68	356	0.10422	3.94279	58.34	−76	0.025
0.03	0.52	391	0.01078	5.09605	517.718	−116.6	0.00723
0.04	0.37	447	0.00767	7.605	704.5	−129.4	0.00313
0.06	0.44	417	0.02725	6.1972	535.22	−95.8	0.00691



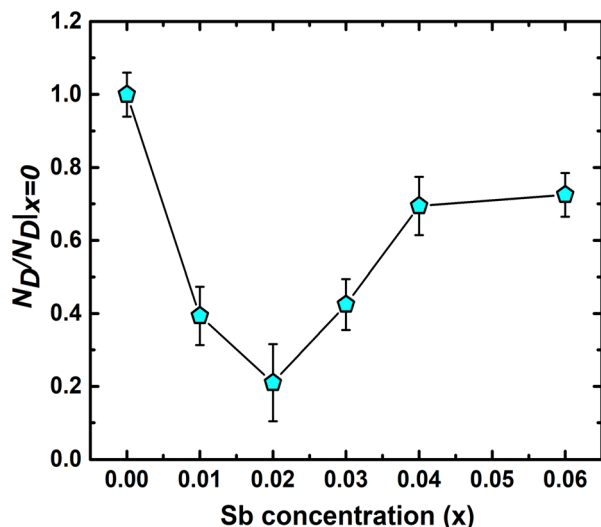


Fig. 9 Relative dislocation density ( $N_D/N_{D|x=0}$ ) for the  $\text{TiCoSb}_{1+x}$  ( $x = 0, 0.01, 0.02, 0.03, 0.04, 0.06$ ) polycrystalline samples, estimated from x-ray diffraction data using modified Williamson–Hall equation.

0.02, and the lowest  $N_D$  has been observed for the  $\text{TiCoSb}_{1.02}$  sample. This is in agreement with the previous analysis that the presence of a minimum embedded phase with good crystal quality has been observed for the  $\text{TiCoSb}_{1.02}$  sample amid synthesized samples ( $\text{TiCoSb}_{1+x}$ ;  $x = 0.0, 0.01, 0.02, 0.03, 0.04, 0.06$ ). An increase in the wt% of embedded phases in the synthesized samples may enhance the lattice mismatch at the grain boundary, causing an increment in  $N_D$ .

Temperature dependent  $S(T)$  has indicated all the synthesized samples (Fig. 10(a))  $\text{TiCoSb}_{1+x}$  ( $x = 0.0, 0.01, 0.02, 0.03, 0.04, 0.06$ ) are n-type in nature. The negative value of  $S(T)$  has indicated a majority of carriers are electrons. However, pristine

$\text{TiCoSb}$  should have shown positive  $S(T)$ , i.e., p-type in nature.<sup>79,80</sup> Synthesized samples have shown an n-type nature as Fermi surfaces have been modified due to embedded phases and defects. The magnitude of  $S(T)$  values is different than the previously reported.<sup>43,81,82</sup> However, Sekimoto *et al.* have also reported a similar  $S(T)$  value of  $\text{TiCoSb} \sim -150 \mu\text{V K}^{-1}$  at 350 K.<sup>68</sup> An increase in  $S(T)$  data beyond 275 K may be attributed to thermal excitation of minority carriers at high temperatures.<sup>83</sup> It has been found that  $S(T)$  for  $\text{TiCoSb}$  (i.e.,  $x = 0.00$ ) is nearly zero.  $|S(T)|$  of the synthesized samples,  $\text{TiCoSb}_{1+x}$  ( $0 < x \leq 0.04$ ) increases with increasing Sb concentration. However,  $|S(T)|$  slightly reduces for  $\text{TiCoSb}_{1.06}$ .

The non-monotonic behavior of  $S(T)$  with Sb concentration may be attributed to the band structure modification owing to the presence of defects (vacancy, interstitial, and antisite) and embedded phases (CoTi and CoSb). The thermopower of a semiconductor may be written as<sup>45,84</sup>

$$|S| = \frac{(\sigma_n|S_n| - \sigma_p|S_p|)}{\sigma_n + \sigma_p} \quad (5)$$

Here,  $S_n/S_p$  ( $S_{n,p}$ ) and  $\sigma_n/\sigma_p$  ( $\sigma_{n,p}$ ) are the Seebeck coefficients and the electrical conductivities due to n-type and p-type carriers, respectively. It has been assumed that both types of charge carriers are involved in the conduction process. However,  $S_{n,p}$  may be written as, according to the Mott expression<sup>85,86</sup>

$$|S_{n,p}| = \frac{\pi^2 K_B^2 T}{3e} \left[ \frac{1}{n_{n,p}} \frac{dn_{n,p}(E)}{dE} + \frac{1}{\mu_{n,p}} \frac{d\mu_{n,p}(E)}{dE} \right]_{E \approx E_F} \quad (6)$$

here,  $n_{n,p}$  is energy dependent n-type or p-type carrier density,  $E_F$ ,  $e$ , and  $K_B$  are Fermi energy, electronic charge, and Boltzmann constant. The mobility of n-type or p-type charge carrier has been denoted as  $\mu_{n,p}$ . Further, energy dependent  $n_{n,p}(E)$  is related with

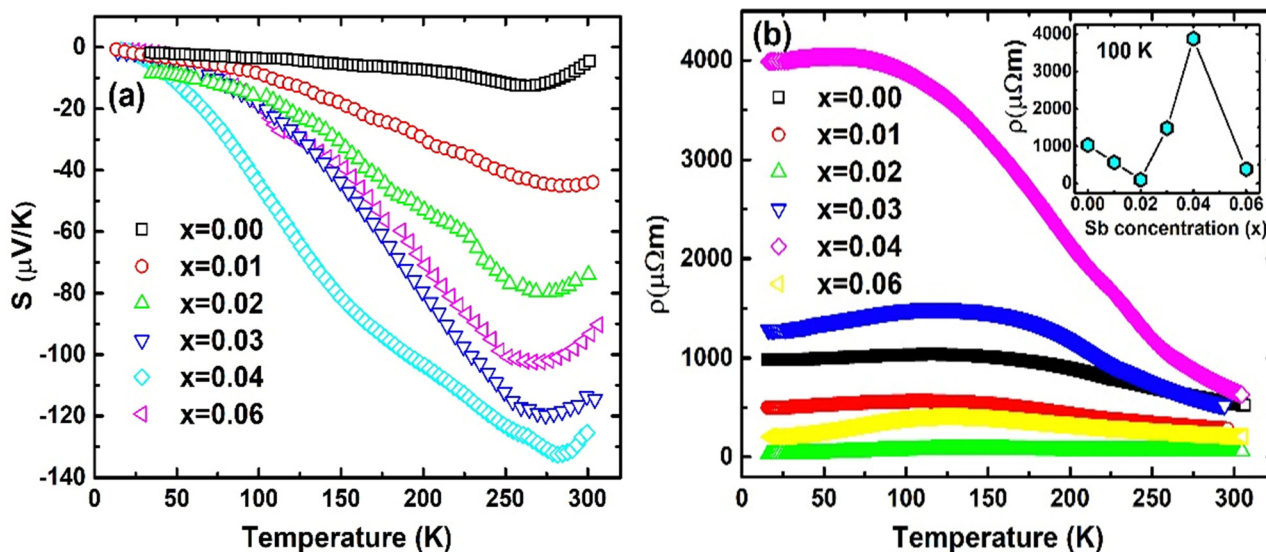


Fig. 10 Temperature dependent (a) Seebeck coefficient  $S(T)$  and (b) electrical resistivity  $\rho(T)$  of  $\text{TiCoSb}_{1+x}$  ( $x = 0.0, 0.01, 0.02, 0.03, 0.04, 0.06$ ) half-Heusler alloy. (Inset of (b) indicates Sb concentration dependent  $\rho$  at 100 K).





DOS,  $n_{n,p}(E) = g_{c,v}(E)f(E)$ . Here  $g_{c,v}$  represents DOS in the conduction band/valence band, near the Fermi level and  $f(E)$  is the Fermi distribution function. Thermal variation of  $S(T)$  of synthesized  $\text{TiCoSb}_{1-x}$  is almost zero, indicating compensated behaviour of charge carriers in the conduction processes according to eqn (5). However,  $S(T)$  for the  $\text{TiCoSb}_{1+x}$  ( $0 \leq x \leq 0.04$ ) may be explained according to the Mott expression (eqn (6)). Theoretical calculation of band structure and DOS suggest that Ti and Co atoms mainly contribute to the conduction and valence bands of  $\text{TiCoSb}$ , respectively. It should be recalled from the Rietveld refinement data that Co vacancies have increased with Sb concentration for the synthesized samples (Fig. 6). Hence, Co vacancies in the  $\text{TiCoSb}$  crystal directly contribute to the DOS in the valence band of  $\text{TiCoSb}$ . As Co vacancy is created, DOS in the valence band near  $E_F$  decreases. Energy dependent  $n_p(E \sim E_F)$  may decrease, owing to the local decrease in DOS in the valence band ( $g_v(E)$ ) near the  $E_F$ . It causes a decrease in  $|S_p|$  in the synthesized samples. Further, carriers near the  $E_F$  mostly contribute to the conduction.  $\sigma = ne\mu$  indicates that a drop in  $n_p(E \sim E_F)$  near  $E_F$  may cause a decrease in  $\sigma_p$  and a concomitant reduction in  $\sigma_{\text{tot}}$ . Hence, the resultant  $|S(T)|$ , according to eqn (6) for  $\text{TiCoSb}_{1+x}$  ( $0 \leq x \leq 0.04$ ), have enhanced, provided the  $E_F$  of the materials aligns properly. Maximum wt% of CoSb embedded phases along with interstitial Sb have been obtained for the  $\text{TiCoSb}_{1.06}$  sample. The position of the DOS-peak for CoSb embedded phases exactly matches the position of DOS at the valence band of  $\text{TiCoSb}$ .<sup>87</sup> The complex interplay of interstitial Sb atom and DOS of CoSb support the increase in DOS at the valence band of  $\text{TiCoSb}_{1.06}$  sample and results in a slight decrease in  $S(T)$ .

$\rho(T)$  of all the synthesized samples,  $\text{TiCoSb}_{1+x}$  ( $x = 0.0, 0.01, 0.02, 0.03, 0.04, 0.06$ ) has been depicted in Fig. 10(b). Non-monotonic thermal variations of  $\rho(T)$  indicate that the synthesized  $\text{TiCoSb}_{1+x}$  ( $x = 0.0, 0.01, 0.02, 0.03, 0.04, 0.06$ ) samples are semiconducting in nature.  $\rho(T)$  decreases with increasing Sb concentration for  $0 \leq x \leq 0.02$ . However, further increase of extra Sb causes increase in  $\rho(T)$  ( $0.02 \leq x \leq 0.04$ ) and the highest  $\rho(T)$  is observed for the  $x = 0.04$  sample.  $\rho(T)$  at 300 K of the synthesized samples has been presented in Table 2.  $\rho(T)$  of  $\text{TiCoSb}_{1.02}$  is similar to the previously reported value for pristine  $\text{TiCoSb}$ .<sup>68</sup> Increase in  $\rho(T)$  with Sb concentration for  $\text{TiCoSb}_{1+x}$  samples may be related to the inherent Co vacancy in the synthesized samples. In the preceding discussion, it has been observed that Co vacancy may lead to a decrease in  $\sigma_{\text{tot}}$  ( $= \sigma_n + \sigma_p$ ) due to a change in DOS at the valence band. However, embedded phases, defects, and disorder also play crucial roles in the conduction of carrier.<sup>88,89</sup> Embedded phases in the  $\text{TiCoSb}$  host phases may act as scattering centre during the conduction processes. In order to get insight into scattering, e-e and e-ph scattering coefficients have been estimated from the  $\rho(T)$  data. The  $\rho(T)$  data has been fitted with equation  $\rho(T) = \rho_0 + AT + BT^2$  at low temperature ( $T < 150$  K), where  $A$  and  $B$  represent e-ph and e-e scattering coefficients, respectively.<sup>77,90</sup> Non-monotonic variation of e-e and e-ph have been presented in Fig. 11. e-e and e-ph coefficients have decreased for  $0 \leq x \leq 0.02$  in  $\text{TiCoSb}_{1+x}$  samples, and a sudden drop has been observed for the  $\text{TiCoSb}_{1.02}$  sample. It is

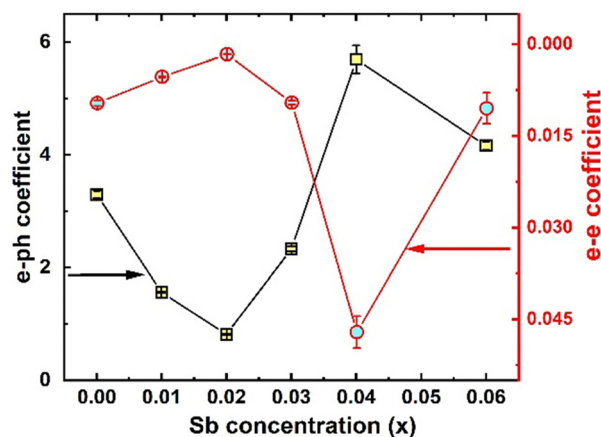


Fig. 11 Variation of electron–phonon (e–ph) and electron–electron (e–e) scattering coefficient with Sb concentration for synthesized  $\text{TiCoSb}_{1+x}$  ( $x = 0.0, 0.01, 0.02, 0.03, 0.04, 0.06$ ) polycrystalline samples, obtained by fitting the temperature dependent resistivity data.

important to mention that the maximum wt% of the  $\text{TiCoSb}$  phase is obtained for  $\text{TiCoSb}_{1.02}$  and crystal quality increases for the  $\text{TiCoSb}_{1.02}$  sample. The decrease in wt% of  $\text{TiCoSb}$  phase and increase in Co vacancy along with embedded phases increase the scattering center of the synthesized samples  $\text{TiCoSb}_{1+x}$  ( $0.02 \geq x > 0$  and  $0.02 \leq x \leq 0.04$ ). The highest wt% of the  $\text{TiCoSb}$  phase has been obtained for the  $\text{TiCoSb}_{1.02}$  sample, and correspondingly lowest  $\rho(T)$  has been observed. Embedded phases and Co vacancy increase for  $x = 0.03$  and  $0.04$ , which corroborated with the increase in  $\rho(T)$ . A sudden drop in  $\rho(T)$  for  $\text{TiCoSb}_{1.06}$  may be related to the change in the band structure and formation of the impurity band, owing to excessive impurity phases and interstitial atoms.

The power factor, PF ( $S^2\sigma$ ) of the synthesized samples has been estimated using  $S$ - $T$  and  $\rho$ - $T$  data. ‘PF versus temperature’ data of  $\text{TiCoSb}_{1+x}$  are depicted in Fig. S4 (ESI<sup>†</sup>). Non-monotonic thermal variation of power factor is observed. The highest power factor is obtained for  $\text{TiCoSb}_{1.02}$  at 300 K.

In order to get the flavour of change in  $ZT$  due to embedded phases and defects, thermal conductivity  $\kappa$  ( $\kappa = \kappa_e + \kappa_L$ ,  $\kappa_e$  = electronic thermal conductivity and  $\kappa_L$  = lattice thermal conductivity) has been estimated.  $\kappa_e$  has been estimated using the well-known Wiedemann Franz law,  $\kappa_e = L\sigma T$  ( $L$  is the Lorenz number). Further,  $L$  has been calculated from the temperature dependent  $S(T)$  data, employing the relation  $L = [1.5 + \exp(-|S|/116)] \times 10^{-8}$ .<sup>91</sup>  $\kappa_L$  is directly related to the phonon scattering mechanism *viz.*, phonon–phonon scattering due to defects. Heat conduction has been performed by acoustic phonons, and the Umklapp process is dominant in the phonon scattering at high temperature. However, according to Slack,  $\kappa_L$  may be written in the limit Umklapp scattering processes<sup>92</sup>

$$\kappa_L = A \frac{\bar{M}\theta_D^3\delta}{\gamma_G^3 n^{2/3} T} \quad (7)$$

where,  $\bar{M}$ ,  $\delta^3$  and  $n$  are the average atomic mass in the unit cell, volume per atom, and number of atoms in the primitive cell,



respectively. There are 12 atoms per unit cell of TiCoSb, *i.e.*,  $n = 12$  and  $\Lambda \sim 3.1 \times 10^{-6}$  (a physical constant). The value of the Gruneisen parameter  $\gamma_G$  of pristine TiCoSb has been considered to estimate  $\kappa_L$  of the synthesized samples using eqn (7). It is important to note that  $\gamma_G$  is almost temperature independent and depends on the stoichiometry of the constituent elements. In this study, we are dealing with TiCoSb material with a very small variation of Sb in stoichiometry. Hence,  $\gamma_G$  of TiCoSb, *i.e.*, 2.13, has been considered for calculation of  $\kappa_L$  using eqn (7).<sup>32</sup>  $ZT$  of the synthesized samples has been estimated using equation  $ZT = S^2\sigma T/\kappa$ . The value of  $\theta_D$ , estimated using Rietveld refinement and  $\kappa_L$  of the synthesized samples have been presented in Table 2. Fig. 12 represents the dependency of  $ZT$  on extra Sb concentration in TiCoSb<sub>1+x</sub> at room temperature. It is crucial to mention that a drastic change in  $ZT$  has been observed for the TiCoSb<sub>1.02</sub> sample. Maximum  $ZT \sim 0.025$  has been observed for the TiCoSb<sub>1.02</sub> sample, which is nearly 4 to 5 times higher than the previously reported values for the pristine TiCoSb at room temperature.<sup>40,42,54–56</sup>

To make the present communication a self-contained one, here, we make a brief comparison of our results with the previously reported TE responses and some possible functional elements that can be utilized for energy conversion. For instance, we want to highlight ZrNiSb, HfNiSb, and ScCoSb alloys.<sup>25</sup> These are metallic and crystallize in the TiNiSi structure type. ScCoSb and ZrNiSb show no band gap in the vicinity of the Fermi level, whereas TiCoSb exhibits  $E_g \sim 1.03$  eV. TE studies are not reported for HfNiSb and ZrNiSb alloys, to date, to the best of our concerns. However, it seems that materials may show poor TE performance related to TiCoSb due to their metallic nature.  $ZT \sim 0.009$  is reported for ScCoSb HH alloy at 380 K,<sup>93</sup> and our synthesized sample shows better TE performance and almost 2.6 times higher value is reported in the current work. Asaad *et al.* have reported  $ZT \sim 0.01$  for TiCoSb-based HH alloy at room temperature.<sup>54</sup>  $ZT \sim 0.005$  is reported by Birkel *et al.* for TiCoSb HH alloy at room temperature, prepared by arc-melting.<sup>55</sup> Comparing the earlier results,

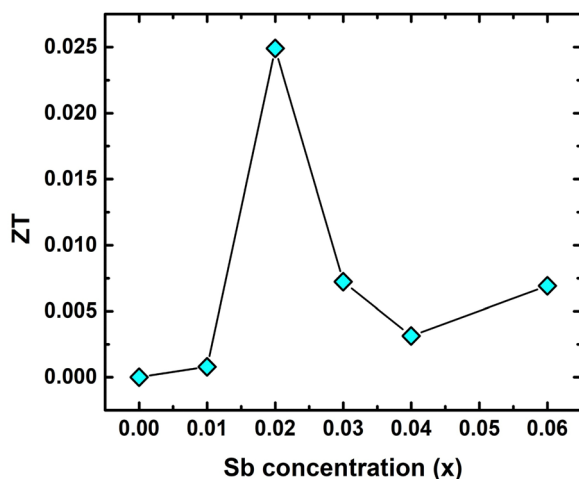


Fig. 12 Room temperature  $ZT$  of TiCoSb<sub>1+x</sub> ( $x = 0.0, 0.01, 0.02, 0.03, 0.04, 0.06$ ) half-Heusler alloy.

we can safely argue that our functional element is quite superior for energy conversion.

## V. Conclusion

In conclusion, the effect of embedded phases and defects on structural, resistive, and thermopower of TiCoSb HH polycrystalline material have been reported. Theoretical calculations have been employed to estimate the DOS, band structure, and formation energy for the vacancy, anti-site, and interstitial defects. Six samples of TiCoSb<sub>1+x</sub> ( $x = 0.0, 0.01, 0.02, 0.03, 0.04, 0.06$ ) have been synthesized using solid state reaction method, followed by arc-melting. Excess Sb has been added to TiCoSb stoichiometry to compensate for the evaporated Sb and create vacancies and embedded phases during the arc melting of the constituent elements. Mix-phase Rietveld refinement analysis of the XRD data clearly reveals the presence of CoTi and CoSb phases. Optimization of CoTi and CoSb phases and maximum wt% of TiCoSb are observed for TiCoSb<sub>1.02</sub>. A distinct slope change is observed at 2% extra Sb concentration for 'wt% of TiCoSb' versus the 'Sb concentration' graph. Co vacancy increases with Sb concentration obtained from Rietveld refinement and schematically presented using VESTA software.  $\theta_D$  employing  $B_{iso}$ , obtained from XRD data of the synthesized samples has been estimated and  $\theta_D$  of TiCoSb<sub>1.02</sub> matches with reported value. Lattice strain ( $\epsilon$ ) and grain size ( $d$ ) have been estimated by Williamson–Hall plots. Minimum  $\epsilon$  and maximum  $d$  are obtained for 2% extra Sb contained sample due to improved crystal quality and maximum TiCoSb phase. It also supports the minimum  $N_D$  for the TiCoSb<sub>1.02</sub> sample.  $S(T)$  and  $\rho(T)$  are related to the modification of DOS owing to the Co vacancy and embedded phases, explained by the Mott equation. The e–e and e–ph scattering coefficients are correlated with the defects and the embedded phases. PF has been estimated using  $\rho(T)$  and  $S(T)$  data. In order to get the flavour of  $ZT$ ,  $\kappa_L$  and  $\kappa_e$  are calculated from XRD and resistivity data using temperature dependent Lorentz number obtained from  $S(T)$ . However, the final conclusion may be drawn after the detailed analysis of the experimental data of  $\kappa$ .  $ZT$  of TiCoSb strongly depends on extra Sb added to stoichiometry during synthesis. It has been observed that the  $ZT$  of the TiCoSb<sub>1.02</sub> sample is 4 to 5 times greater than previously reported values for TiCoSb at room temperature. Corroborated structural and transport data reveal that the best pristine phase of TiCoSb and greater TE properties of TiCoSb is obtained for 2% extra Sb contained sample. Hence, 2% extra Sb in TiCoSb stoichiometry is sufficient to compensate the loss of Sb during synthesis. The resistivity and thermopower of TiCoSb are influenced due to the modification in DOS near the Fermi surface by defects and embedded phases.

## Conflicts of interest

There are no conflicts to declare.



## Acknowledgements

This work is supported by the Science and Engineering Research Board (SERB), Government of India, in the form of sanctioning research project (File Number: EEQ/2018/001224). We acknowledge UGC DAE CSR, Kolkata, for providing arc melting facilities. Author SM is thankful to CSIR, India for providing Research Fellowships (File Number: 08/463(0002)/2019-EMR-I).

## References

- 1 F. Zelenka, P. Brož, J. Vřešťál, J. Buršík, A. Zemanová, G. Rogl and P. Rogl, *CALPHAD*, 2021, **74**, 102292.
- 2 P. Larson, S. D. Mahanti and M. G. Kanatzidis, *Phys. Rev. B: Condens. Matter Mater. Phys.*, 2000, **62**, 12754.
- 3 S.-Y. Lin, M. Chen, X.-B. Yang, Y.-J. Zhao, S.-C. Wu, C. Felser and B. Yan, *Phys. Rev. B: Condens. Matter Mater. Phys.*, 2015, **91**, 094107.
- 4 W. Al-Sawai, H. Lin, R. S. Markiewicz, L. A. Wray, Y. Xia, S. Y. Xu, M. Z. Hasan and A. Bansil, *Phys. Rev. B: Condens. Matter Mater. Phys.*, 2010, **82**, 125208.
- 5 H. Shi, W. Ming, D. S. Parker, M.-H. Du and D. J. Singh, *Phys. Rev. B*, 2017, **95**, 195207.
- 6 S. Chadov, X. Qi, J. Kübler, G. H. Fecher, C. Felser and S. C. Zhang, *Nat. Mater.*, 2010, **9**, 541.
- 7 Z. Hou, W. Wang, G. Xu, X. Zhang, Z. Wei, S. Shen, E. Liu, Y. Yao, Y. Chai and Y. Sun, *et al.*, *Phys. Rev. B: Condens. Matter Mater. Phys.*, 2015, **92**, 235134.
- 8 N. S. Chauhan, S. Bathula, A. Vishwakarma, R. Bhardwaj, K. K. Johari, B. Gahtori and A. Dhar, *J Materiomics*, 2019, **5**, 94.
- 9 H. Lin, L. A. Wray, Y. Xia, S. Xu, S. Jia, R. J. Cava, A. Bansil and M. Z. Hasan, *Nat. Mater.*, 2010, **9**, 546.
- 10 S. LeBlanc, *Sustain. Mater. Technol.*, 2014, **1–2**, 26.
- 11 S. Bentouba, N. Zioui, P. Breuhaus and M. Bourouis, *Energies*, 2023, **16**, 5193.
- 12 R. J. Quinn and J.-W. G. Bos, *Mater. Adv.*, 2021, **2**, 6246.
- 13 S. J. Poon, D. Wu, S. Zhu, W. Xie, T. M. Tritt, P. Thomas and R. Venkatasubramanian, *J. Mater. Res.*, 2011, **26**, 2795.
- 14 S. Populoh, O. C. Brunko, K. Gałazka, W. Xie and A. Weidenkaff, *Materials*, 2013, **6**, 1326.
- 15 Y. Sargolzaeiaval, V. Padmanabhan Ramesh, T. V. Neumann, V. Misra, D. Vashae, M. D. Dickey and M. C. Öztürk, *Appl. Energy*, 2020, **262**, 114370.
- 16 M. Hyland, H. Hunter, J. Liu, E. Veety and D. Vashae, *Appl. Energy*, 2016, **182**, 518.
- 17 H. Zhu, W. Li, A. Nozariasbmarz, N. Liu, Y. Zhang, S. Priya and B. Poudel, *Nat. Commun.*, 2023, **14**, 3300.
- 18 Y. Li, J. Li, J. Du, C. Zhang, X. Wang, Q. Xiang and C. Zhang, *Nucl. Instrum. Methods Phys. Res., Sect. B*, 2020, **479**, 55.
- 19 J. Yang and T. Caillat, *MRS Bull*, 2006, **31**, 224.
- 20 A. Witze, *Nature*, 2014, **515**, 484.
- 21 K. Elphick, W. Frost, M. Samiepour, T. Kubota, K. Takanashi, H. Sukegawa, S. Mitani and A. Hirohata, *Sci. Technol. Adv. Mater.*, 2021, **22**, 235.
- 22 M. P. Ghimire, Sandeep, T. P. Sinha and R. K. Thapa, *J. Alloys Compd.*, 2011, **509**, 9742.
- 23 V. Ksenofontov, G. Melnyk, M. Wojcik, S. Wurmehl, K. Kroth, S. Reiman, P. Blaha and C. Felser, *Phys. Rev. B: Condens. Matter Mater. Phys.*, 2006, **74**, 134426.
- 24 F. Casper, T. Graf, S. Chadov, B. Balke and C. Felser, *Semicond. Sci. Technol.*, 2012, **27**, 063001.
- 25 H. Kleinke and C. Felser, *J. Solid State Chem*, 1999, **144**, 330.
- 26 H. Kleinke and Z. Anorg Allg, *Chem*, 1998, **624**, 1771.
- 27 M. Zhou, L. Chen, C. Feng, D. Wang and J.-F. Li, *J. Appl. Phys*, 2007, **101**, 113714.
- 28 P. Qiu, X. Huang, X. Chen and L. Chen, *J. Appl. Phys*, 2009, **106**, 103703.
- 29 K. Xia, P. Nan, S. Tan, Y. Wang, B. Ge, W. Zhang, S. Anand, X. Zhao, G. J. Snyder and T. Zhu, *Energy Environ. Sci.*, 2019, **12**, 1568.
- 30 T. Graf, C. Felser and S. S. P. Parkin, *Prog. Solid. State Ch.*, 2011, **39**, 1.
- 31 P. Paufler, *Cryst. Res. Technol.*, 1987, **22**, 1436.
- 32 H. Joshi, D. P. Rai, A. Laref and R. K. Thapa, *Mater. Res. Express*, 2019, **6**, 066307.
- 33 J. Tobola, J. Pierre, S. Kaprzyk, R. V. Skolozdra and M. A. Kouacou, *J. Phys.: Condens. Matter*, 1998, **10**, 1013.
- 34 S. Ögüt and K. M. Rabe, *Phys. Rev. B: Condens. Matter Mater. Phys.*, 1995, **51**, 10443.
- 35 J. Toboła and J. Pierre, *J. Alloys Compd.*, 2000, **296**, 243.
- 36 S. Anand, K. Xia, V. I. Hegde, U. Aydemir, V. Kocovski, T. Zhu, C. Wolverton and G. J. Snyder, *Energy Environ. Sci.*, 2018, **11**, 1480.
- 37 H. Beyer, J. Nurnus, H. Böttner, A. Lambrecht, E. Wagner and G. Bauer, *Physica E Low Dimens. Syst. Nanostruct.*, 2002, **13**, 965.
- 38 M. Tan, L. Hao, H. Li, C. Li, X. Liu, D. Yan, T. Yang and Y. Deng, *Sci. Rep.*, 2020, **10**, 5978.
- 39 V. K. Zaitsev, M. I. Fedorov, E. A. Gurieva, I. S. Eremin, P. P. Konstantinov, A. Y. Samunin and M. V. Vedernikov, *Phys. Rev. B: Condens. Matter Mater. Phys.*, 2006, **74**, 045207.
- 40 M. Zhou, C. Feng, L. Chen and X. Huang, *J. Alloys Compd.*, 2005, **391**, 194.
- 41 M. Terada, K. Endo, Y. Fujita and R. Kimura, *J. Phys. Soc. Jpn.*, 1972, **32**, 91.
- 42 T. Sekimoto, K. Kurosaki, H. Muta and S. Yamanaka, *J. Alloys Compd.*, 2006, **407**, 326.
- 43 H. Joshi, D. P. Rai, L. Hnamte, A. Laref and R. K. Thapa, *Heliyon*, 2019, **5**, e01155.
- 44 S. Chen and Z. Ren, *Mater. Today*, 2013, **16**, 387.
- 45 T. Wu, W. Jiang, X. Li, Y. Zhou and L. Chen, *J. Appl. Phys*, 2007, **102**, 103705.
- 46 Y. Stadnyk, Y. Gorelenko, A. Tkachuk, A. Goryn, V. Davydov and O. Bodak, *J. Alloys Compd.*, 2001, **329**, 37.
- 47 B. Dongre, J. Carrete, S. Wen, J. Ma, W. Li, N. Mingo and G. K. H. Madsen, *J. Mater. Chem. A*, 2020, **8**, 1273.
- 48 K. Xia, Y. Liu, S. Anand, G. J. Snyder, J. Xin, J. Yu, X. Zhao and T. Zhu, *Adv. Funct. Mater.*, 2018, **28**, 1705845.
- 49 F. Aliev, N. Brandt, V. Kozyr'Kov, V. Moshchalkov, R. Skolozdra, Y. V. Stadnyk and V. Pecharskii, *JETP Lett*, 1987, **45**, 684.



- 50 F. G. Aliev, N. B. Brandt, V. V. Moshchalkov, V. V. Kozyrkov, R. V. Skolozdra and A. I. Belogorokhov, *Z. Phys. B: Condens. Matter*, 1989, **75**, 167.
- 51 P. Qiu, J. Yang, X. Huang, X. Chen and L. Chen, *Appl. Phys. Lett.*, 2010, **96**, 152105.
- 52 L. Chen, X. Zeng, T. M. Tritt and S. J. Poon, *J. Electron. Mater.*, 2016, **45**, 5554.
- 53 Q. Wang, X. Xie, S. Li, Z. Zhang, X. Li, H. Yao, C. Chen, F. Cao, J. Sui and X. Liu, *et al.*, *J. Materiomics*, 2021, **7**, 756.
- 54 M. Asaad, J. Buckman and J.-W. G. Bos, *Metals*, 2018, **8**, 935.
- 55 C. S. Birkel, W. G. Zeier, J. E. Douglas, B. R. Lettiere, C. E. Mills, G. Seward, A. Birkel, M. L. Snedaker, Y. Zhang and G. J. Snyder, *et al.*, *Chem. Mater.*, 2012, **24**, 2558.
- 56 S.-C. Ur, *Korean J. Mater. Res.*, 2011, **21**, 542.
- 57 Y. Xia, V. Ponnambalam, S. Bhattacharya, A. L. Pope, S. J. Poon and T. M. Tritt, *J. Phys.: Condens. Matter.*, 2001, **13**, 77.
- 58 V. D. Mote, Y. Purushotham and B. N. Dole, *J. Theor. Appl. Phys.*, 2012, **6**, 6.
- 59 S. Das, P. Singha, V. A. Kulbachinskii, V. G. Kytin, G. Das, S. Janaky, A. K. Deb, S. Mukherjee, A. Maignan and S. Hebert, *et al.*, *J. Materiomics*, 2021, **7**, 545.
- 60 J. Rodríguez-Carvajal, *Phys. B*, 1993, **192**, 55.
- 61 S. Mahakal, D. Das, A. Jana, A. Banerjee and K. Malik, *J. Phys. Conf. Ser.*, 2020, 012020.
- 62 W. H. Kettler, R. Wernhardt and M. Rosenberg, *Rev. Sci. Instrum.*, 1986, **57**, 3053.
- 63 S. Skipidarov and M. Nikitin, *Thermoelectrics for Power Generation*, IntechOpen, Rijeka, 2016.
- 64 G. Kresse and J. Furthmüller, *Comput. Mater. Sci.*, 1996, **6**, 15.
- 65 J. P. Perdew, K. Burke and M. Ernzerhof, *Phys. Rev. Lett.*, 1996, **77**, 3865.
- 66 P. E. Blöchl, *Phys. Rev. B: Condens. Matter Mater. Phys.*, 1994, **50**, 17953.
- 67 P. J. Webster and K. R. A. Ziebeck, *J. Phys. Chem. Solids*, 1973, **34**, 1647.
- 68 T. Sekimoto, K. Kurosaki, H. Muta and S. Yamanaka, *J. Alloys Compd.*, 2005, **394**, 122.
- 69 K. Momma and F. Izumi, *J. Appl. Crystallogr.*, 2008, **41**, 653.
- 70 D. Das, K. Malik, S. Das, P. Singha, A. K. Deb, V. A. Kulbachinskii, R. Basu, S. Dhara, A. Dasgupta and S. Bandyopadhyay, *et al.*, *AIP Adv.*, 2018, **8**, 125119.
- 71 P. Fischer, I. Sosnowska and M. Szymanski, *J. Phys. C: Solid State Phys.*, 1978, **11**, 1043.
- 72 I. Skovsen, L. Bjerg, M. Christensen, E. Nishibori, B. Balke, C. Felser and B. B. Iversen, *Dalton Trans.*, 2010, **39**, 10154.
- 73 T. Sekimoto, K. Kurosaki, H. Muta and S. Yamasaka, in *ICT 2005. 24th International Conference on Thermoelectrics, 2005.2005*), pp. 347.
- 74 A. Vishwakarma, N. S. Chauhan, R. Bhardwaj, K. K. Johari, S. R. Dhakate, B. Gahtori and S. Bathula, *Intermetallics*, 2020, **125**, 106914.
- 75 E. O. Hall, *Proc. Phys. Soc. B*, 1951, **64**, 747.
- 76 N. J. Petch, *J. Iron Steel Res. Int.*, 1953, **174**, 4.
- 77 S. Mahakal, D. Das, P. Singha, N. Rana, S. Mukherjee, A. Banerjee and K. Malik, *J. Phys.: Conf. Ser.*, 2022, **2349**, 012022.
- 78 T. Ungár, S. Ott, P. G. Sanders, A. Borbély and J. R. Weertman, *Acta Mater.*, 1998, **46**, 3693.
- 79 A. K. Verma, K. K. Johari, P. Dubey, D. K. Sharma, S. Kumar, S. R. Dhakate, C. Candolfi, B. Lenoir and B. Gahtori, *ACS Appl. Mater. Interfaces*, 2023, **15**, 942.
- 80 F. Serrano-Sanchez, M. Yao, B. He, D. Chen, A. Gloskovskii, A. Fedorov, G. Auffermann, E. Liu, U. Burkhardt and G. H. Fecher, *et al.*, *Nanoscale*, 2022, **14**, 10067.
- 81 J. L. Baker, R. S. Kumar, C. Park, N. Velisavljevic and A. Cornelius, *Intermetallics*, 2018, **95**, 137.
- 82 T. Wu, W. Jiang, X. Li, S. Bai, S. Liufu and L. Chen, *J. Alloys Compd.*, 2009, **467**, 590.
- 83 P. Singha, S. Das, V. A. Kulbachinskii, V. G. Kytin, A. S. Apreleva, D. J. Voneshen, T. Guidi, A. V. Powell, S. Chatterjee and A. K. Deb, *et al.*, *J. Appl. Phys.*, 2021, **129**, 055108.
- 84 J. Yang, D. T. Morelli, G. P. Meisner, W. Chen, J. S. Dyck and C. Uher, *Phys. Rev. B: Condens. Matter Mater. Phys.*, 2003, **67**, 165207.
- 85 R. Moshwan, L. Yang, J. Zou and Z.-G. Chen, *Adv. Funct. Mater.*, 2017, **27**, 1703278.
- 86 M. Cutler and N. F. Mott, *Phys. Rev.*, 1969, **181**, 1336.
- 87 W. Ding, J. Zeng, W. Qin, P. Cui and Z. Zhang, *Phys. Rev. Lett.*, 2020, **124**, 027002.
- 88 K. W. Böer and U. W. Pohl, in *Semiconductor Physics*, ed. K. W. Böer, and U. W. Pohl, Springer International Publishing, Cham, 2018, pp. 1053.
- 89 T. Leijtens, G. E. Eperon, A. J. Barker, G. Grancini, W. Zhang, J. M. Ball, A. R. S. Kandada, H. J. Snaith and A. Petrozza, *Energy Environ. Sci.*, 2016, **9**, 3472.
- 90 M. M. Mallick and S. Vitta, *J. Alloys Compd.*, 2017, **710**, 191.
- 91 H.-S. Kim, Z. M. Gibbs, Y. Tang, H. Wang and G. J. Snyder, *APL Mater.*, 2015, **3**, 041506.
- 92 G. A. Slack, *Solid State Phys.*, 1979, **34**, 1.
- 93 A. V. Morozkin and V. N. Nikiforov, *J. Alloys Compd.*, 2005, **400**, 62.

